Zonal overturning circulation and heat flux induced by heaving modes in the world oceans

Article *in* Acta Oceanologica Sinica -English Edition- · November 2015

DOI: 10.1007/s13131-015-0751-3

4 authors, including:

Wei Tan

First Institute of Oceanography

5 PUBLICATIONS **6** CITATIONS

Weiqiang Wang

Chinese Academy of Sciences

26 PUBLICATIONS **282** CITATIONS

Xin Wang

South China Sea Institute of Oceanology, CAS

41 PUBLICATIONS **530** CITATIONS

Acta Oceanol. Sin., 2015, Vol. 34, No. 11, P. 80–91
DOI: 10.1007/s13131-015-0751-3
http://www.hyxb.org.cn
E-mail: hyxbe@263.net

Zonal overturning circulation and heat flux induced by heaving modes in the world oceans

TAN Wei[1], HUANG Rui Xin[2, 3]*, WANG Weiqiang[2], WANG Xin[2]
[1] Hohai University, Nanjing 210098, China
[2] State Key Laboratory of Tropical Oceanography, South China Sea Institute of Oceanology, Chinese Academy of Sciences, Guangzhou 510301, China
[3] Woods Hole Oceanographic Institution, Woods Hole, MA 02543, USA

Received 8 May 2015; accepted 14 July 2015

Abstract
Zonal overturning circulation (ZOC) and its associated zonal heat flux (ZHF) are important components of the oceanic circulation and climate system, although these conceptions have not received adequate attentions. Heaving induced by inter-annual and decadal wind stress perturbations can give rise to anomalous ZOC and ZHF. Based on a simple reduced gravity model, the anomalous ZOC and ZHF induced by idealized heaving modes in the world oceans are studied. For example, in a Pacific-like model basin intensified equatorial easterly on decadal time scales can lead to a negative ZOC with a non-negligible magnitude (-0.3×10^6 m^3/s) and a considerable westward ZHF with an amplitude of –11.2 TW. Thus, anomalous ZOC and ZHF may consist of a major part of climate signals on decadal time scales and thus play an important role in the oceanic circulation and climate change.

Key words: adiabatic motions, heaving, wind-driven circulation, zonal overturning circulation, zonal heat flux

Citation: Tan Wei, Huang Rui Xin, Wang Weiqiang, Wang Xin. 2015. Zonal overturning circulation and heat flux induced by heaving modes in the world oceans. Acta Oceanologica Sinica, 34(11): 80–91, doi: 10.1007/s13131-015-0751-3

1 Introduction

The oceanic general circulation can be conceptually separated into two components: the wind-driven circulation and thermohaline circulation. Wind-driven circulation occupies the upper kilometer of the world oceans, and it is directly forced by wind stress, but it is not directly linked to the stratification in the ocean. In fact, wind-driven circulation can exist in a homogeneous ocean and the framework of the classical theory of wind-driven circulation is built up in separation from the thermodynamics.

On the other hand, thermohaline circulation occupies the entire depth of the world oceans, and it is closely linked to density difference induced by the surface thermohaline forcing, such as heat flux and freshwater flux. However, thermohaline circulation is a dissipation system, and its maintenance requires external source of mechanical energy which is supplied by wind stress, tidal dissipation and geothermal heat flux in the world oceans.

Ideally, therefore, wind-driven circulation can be treated as adiabatic motions, but thermohaline circulation is intimately linked to diabatic motions. Circulation in the world oceans is a complicated system, and it involves transport of water masses, heat and freshwater in three dimensional space. To describe such complicated phenomena, many two-dimensional maps, one-dimensional profiles and zero-dimensional indices have been used.

For example, to describe the poleward transport of water mass and heat, the meridional overturning circulation (MOC) and poleward heat flux (PHF) have been widely used in previous studies. Thermohaline circulation plays a crucial role in regulating MOC and PHF; in addition, quasi-horizontal circulation associated with wind-driven gyres in a stratified ocean also play a role in transporting heat poleward, as discussed in many previous studies and textbooks, e.g., Schmitz (1986a, b), Ganachaud and Wunsch (2000), Talley et al. (2011), Talley (2013) and Huang (2010). However, in the steady state, the poleward heat flux is intimately linked to heat transform through the air-sea interface or between water parcels. As such, PHF is directly linked to the diabatic processes in the oceans.

To show the basic pattern of air-sea heat flux and the implied horizontal heat flux in the world oceans, we used the annual mean climatology of surface heat flux data from the GODAS data (Behringer et al., 1998). As shown in Fig. 1, the net air-sea heat flux in the world oceans is spatially non-uniformly distributed. The most outstanding features in this map are the strong heat flux into the cold tongues in the equatorial Pacific and Atlantic Oceans, plus the strong heat release to the atmosphere in both the Kuroshio and Gulf Stream (and the northern North Atlantic Ocean). This map implies that there should be a mechanism in the ocean which transports strong heat flux in both the meridional and zonal directions. In fact, the transport of heat can be identified as the strong PHF and zonal heat flux (ZHF) diagnosed from this dataset, shown in Figs 1b and c. The PHF integrated over the world oceans is poleward in both hemispheres, i.e., it is southward in the Southern Hemisphere (except for a narrow lat-

Foundation item: The CAS/SAFEA International Partnership Program for Creative Research Teams of Chinese Academy of Sciences; the National Natural Science Foundation of China under contract Nos 41422601, 41376024 and 41376025.
*Corresponding author, E-mail: rhuang@whoi.edu

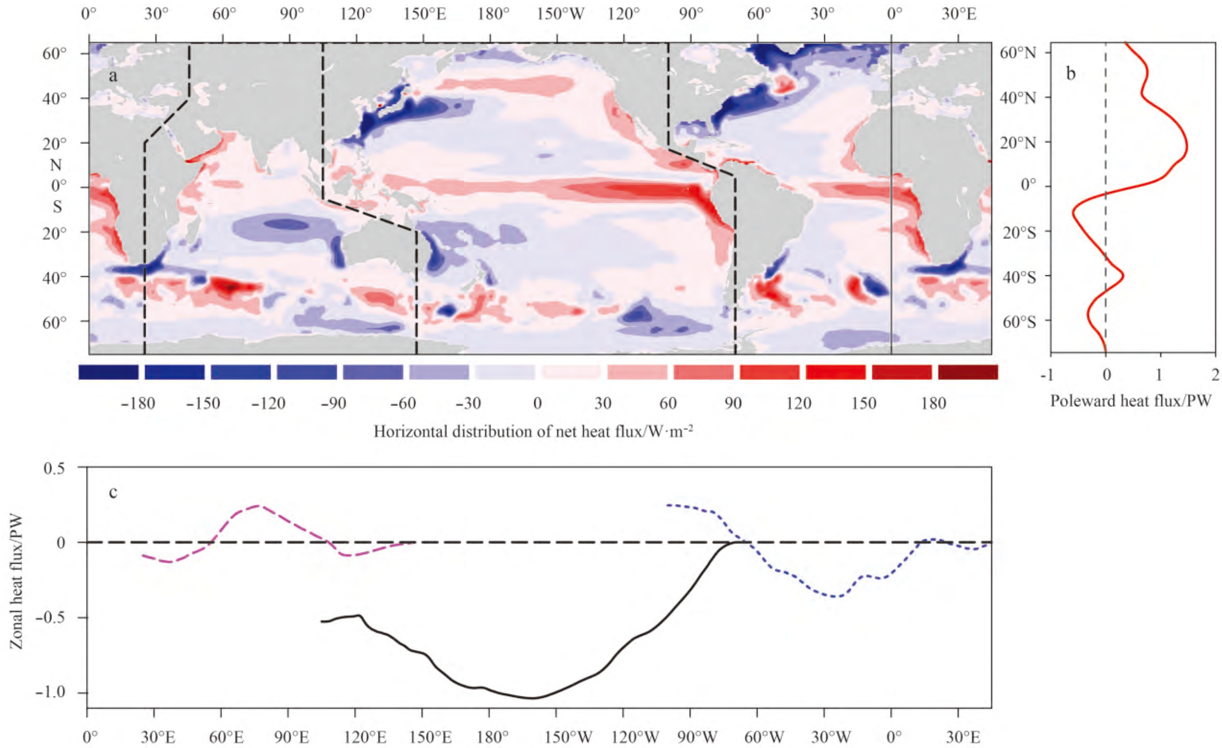

Fig. 1. Annual mean of net air-sea heat flux climatology based on GODAS data (a); meridional heat flux (b) and zonal heat flux (c). See the main text for details.

itude band near 40°S) and northward in the Northern Hemisphere. In the Northern Hemisphere, it reaches the maximum value of 1.5 PW (1 PW=10^{15} W). Note that the PHF is non-zero at the northern boundary of the data domain, indicating that the GODAS heat flux data is taken from a model which domain extends to even higher latitudes.

Because the world oceans are separated into three major basins, except the quasi-periodic channel between 40° and 70°S, we calculate the ZHF for each basin. The ZHF for each basin is defined as zero at the east most grid of each basin, and the eastward heat flux is defined as positive. The boundaries of our calculation are shown in Fig. 1a by the dashed lines. As shown in Fig. 1c, in the steady state, there is huge ZHF in each basin. In both of the Pacific and Atlantic, the ZHF reaches the maximum amplitude of –1.03 PW and –0.36 PW respectively; whereas the ZHF is positive in the middle of the Indian basin, with a maximum value of 0.24 PW. The east-west asymmetric feature of the net air-sea heat flux and the implied ZHF is a critically important issue in the climate system, which has not received adequate attentions. However, we postulate that in the study of climate change, it might be of great interest to examine the variability of the air-sea heat flux and the associated zonal overturning circulation (ZOC) and ZHF.

As discussed above, in the steady state both the PHF and ZHF are closely linked to thermal diffusion across the interface of the ocean-atmosphere or between water parcels; in another word, these are closely linked to diabatic motions in the oceans.

Recently, climate variability related to global environmental changes has been widely discussed, and many investigators explored variability of sea surface temperature, upper ocean heat content, MOC and PHF, e.g., Lyman and Johnson (2008), Lozier et al. (2008), Lozier et al. (2010), Meehl et al. (2011), Meehl et al. (2013). In particular, the dynamic role of wind stress variability on decadal time scale has been explored in several studies, e.g., McGregor et al. (2012), England et al. (2014)

Ideally, perturbations induced by wind stress anomaly can be analyzed in terms of adiabatic motions, without exchange of heat and salt; these motions are called heaving (Bindoff and McDougall, 1994). Physically, changes in stratification can be induced by variability of wind stress, heat and salt exchange. It is to emphasize that the effect of surface forcing anomaly can be transported to the remote areas through adjustment of the global oceanic circulation. For example, wind stress variability near the water mass formation sites can affect the water mass formation rate; through the oceanic currents, such changes will affect the stratification in the world oceans. Therefore, heaving can affect the global ocean even far away from the regime of wind stress anomaly.

Recently, Huang (2015) postulated that adiabatic motions in the ocean induced by wind stress changes can give rise to anomalous MOC, equivalent PHF and vertical heat flux, which might be a non-negligible component of the climate variability diagnosed from observations or computer generated climate datasets.

There is, however, a major issue related to ZOC overlooked in Huang (2015). Although Fig. 1 in Huang (2015) is in fact a sketch about the ZOC, this important issue was not even mentioned in the discussion. This figure is now modified and shown as Fig. 2. Accordingly, if Ekman pumping in a subtropical basin is enhanced, the slope of the thermocline should increase in response; thus, warm water is pushed down in the western basin. However, the total volume of warm water is nearly conserved over such a relatively short time; hence, bottom of the warm water in the eastern basin must rise in compensation. As a result, there is a basin-wide redistribution of warm water in the upper

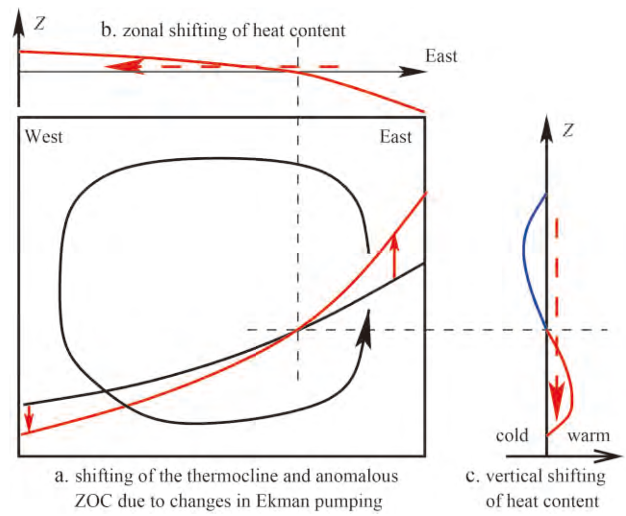

Fig. 2. A schematic of heaving motions in response to strengthened wind stress: a. shifting of the thermocline associated with ZOC; b. zonal shifting of the heat content; and c. vertical shifting of the heat content. This figure is modified from Huang, 2015.

ocean (Fig. 2a). As sketched in Fig. 2, in this process warm water (above the thermocline) in the eastern basin moves upward and it is pushed westward; while warm water in the western basin sinks; therefore, the wind-driven adjustment induces an anomalous ZOC. Consequently, there is also a heat flux in the zonal direction (Fig. 2b) and in the vertical direction (Fig. 2c), i.e., the wind stress induced ZOC should give rise to a ZHF and vertical heat flux.

Therefore, in this study we examine ZOC and ZHF in details. Although in a steady state the PHF and ZHF are mostly due to diabatic motions associated with the thermohaline circulation, in short time scales, from inter-annual to decadal time scale, wind stress perturbations induced heaving motions can give rise to strong anomalous MOC, ZOC, PHF, ZHF and vertical heat flux. The main goal of this study is to examine the ZOC and ZHF associated with decadal climate variability induced by idealized heaving modes in the world oceans. It is clear that this study is a continuation of Huang (2015); thus, to save the space, many technical details of the model settings and experiments are skipped in this paper, and readers interested in such information are referred to Huang (2015).

In the following, a simple two-hemisphere reduced gravity model (2H model) is introduced in Section 2 along with one set of numerical experiments driven by idealized wind stress perturbations. Section 3 describes two numerical experiments for a Southern Hemisphere model (SH model). Finally, we draw the conclusion in Section 4.

2 A two-hemisphere model ocean

2.1 *Model set up*

The 2H model used in this study is a simple reduced gravity model, including two layers, with a constant density of ρ_0 in the upper layer and $\rho_0+\Delta\rho$ in the lower layer. The upper layer thickness is denoted as h, while the lower layer is infinitely deep and assumed motionless. Using the rigid-lid approximation, the pressure contribution of free surface ζ is represented by an equivalent hydrostatic pressure $p=p_a$ at the flat surface z=0. Below the surface, the pressure can be calculated according to the hydrostatic relation. The pressure gradient in the model is described as

$$\nabla p = g'\nabla h\,, \tag{1}$$

where $g'=g\Delta\rho/\rho_0$ is the reduced gravity.

The model ocean is formulated on an equatorial β-plane, and the Coriolis parameter f is defined as

$$f=\beta y, \tag{2}$$

where β=2.236 7×10^{-11} m^{-1}·s^{-1} and y is the meridional distance from the equator. All the parameters in this model are the same as used in Huang (2015). Basic model parameters are specified according climatological data of the world oceans: the reduced gravity is set to 0.015 m/s^2, and the temperature difference between two layers is set to 10 °C (Table 1). In addition, the model is 150° wide in the longitude, and extends from 70°S to 70°N in the latitude with 1°×1° resolution. As in most non-eddy resolving models, this model is based on the B-grid; there are 152×142 grids with a 110-km grid size. The details of the numerical model are referred to Huang (1987).

The zonal wind stress (N/m^2) applied in the 2H model is an idealized function of latitude θ (Fig. 3a):

$$\tau_x = 0.02-0.08\sin(6|\theta|)-0.05[1-\tanh(10|\theta|)]-0.05\left\{1-\tanh\left[10\left(\frac{\pi}{2}-|\theta|\right)\right]\right\}. \tag{3}$$

Table 1. Basic parameters of the models

	Mean depth of the thermocline/m	Reduced gravity/m·s^{-2}	Temperature difference between upper and lower layers/°C	Amplitude of zonal wind stress perturbations/N·m^{-2}
Two-hemisphere model	350	0.015	10.0	0.015
Southern Hemisphere model	750	0.010	7.5	0.020

The model is started from an initial state of rest with the thermocline at a constant depth of 350 m, and run for 300 years to reach a quasi-equilibrium state. Due to the symmetric wind stress, the quasi-equilibrium ocean state is accordingly symmetric to the equator with the bowl-shaped thermocline induced by the Ekman pumping in the subtropical basin and the dome-shaped thermocline induced by the Ekman sucking in the subpolar basin in each hemisphere, Fig. 3b.

2.2 *Numerical experiments*

In this section, a set of numerical experiments are performed. In each experiment the model is restarted from the above mentioned quasi-equilibrium state and forced by additional wind stress perturbations in the form of a Gaussian profile

$$\tau'_x = \Delta\tau e^{-[(y-y_0)/y]^2}, \tag{4}$$

where $\Delta\tau=\pm0.015$ N/m^2 and Δy=1 100 km. Following the notations used in Huang (2015), these 8 experiments are labelled as Exp. 2H-A to Exp. 2H-H, as shown in Fig. 4 and Table 2. In all these experiments, the amplitude of the anomalous wind stress is linearly increased from 0 at the beginning to the specified value at the end of 20 years. Afterward, it is unchanged for additional 20 year simulation.

2.3 *Simulations with wind stress perturbations at the equator*

In Exp. 2H-A (Fig. 4a) the intensified equatorial easterly pushes the warm water in the upper layer westward; thus, the volume of warm water in the western basin increases with time, while it decreases in the eastern basin (Fig. 5a). The volume reduction near the eastern boundary reaches the maximum at 20-year, when the anomalous wind stress reaches the peak; after-

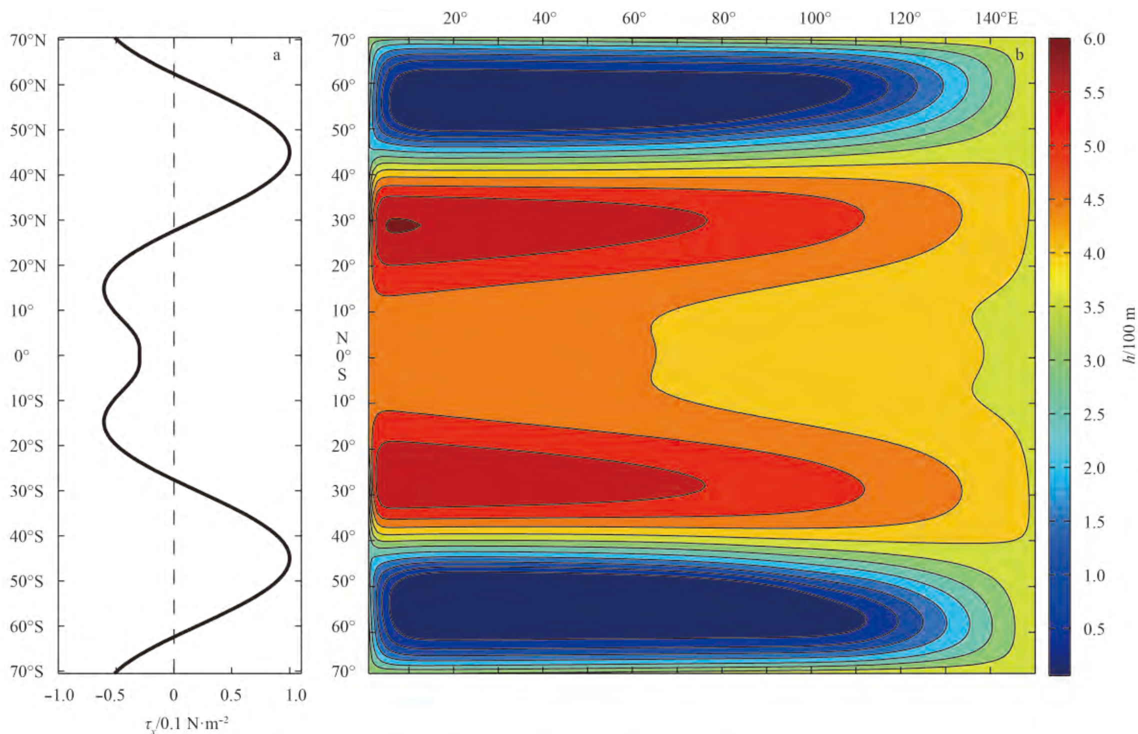

Fig. 3. The quasi-equilibrium state used in the 2H model: a. the zonal wind stress; and b. the depth of the main thermocline.

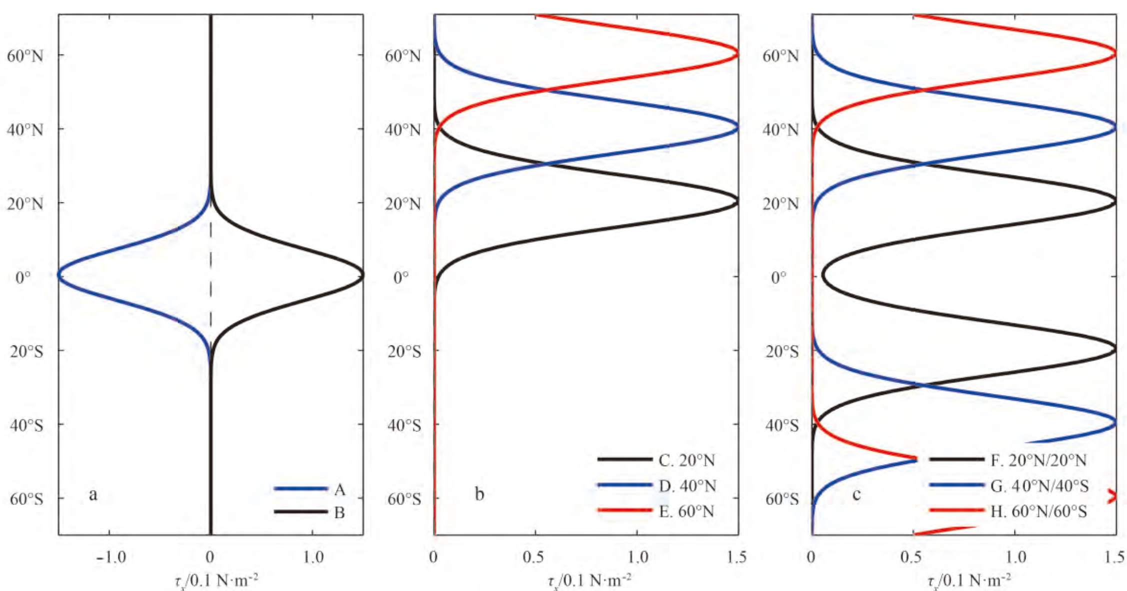

Fig. 4. Wind stress perturbations applied to various latitudes of the model ocean, in unit of 0.1 N/m^2. A. negative anomaly at equator, B. positive anomaly at equator (a); C, D and E. positive anomaly at 20°N, 40°N and 60°N (b); F, G and H. positive anomaly at 20°N/20°S, 40°N/40°S and 60°N/60°S (c), respectively.

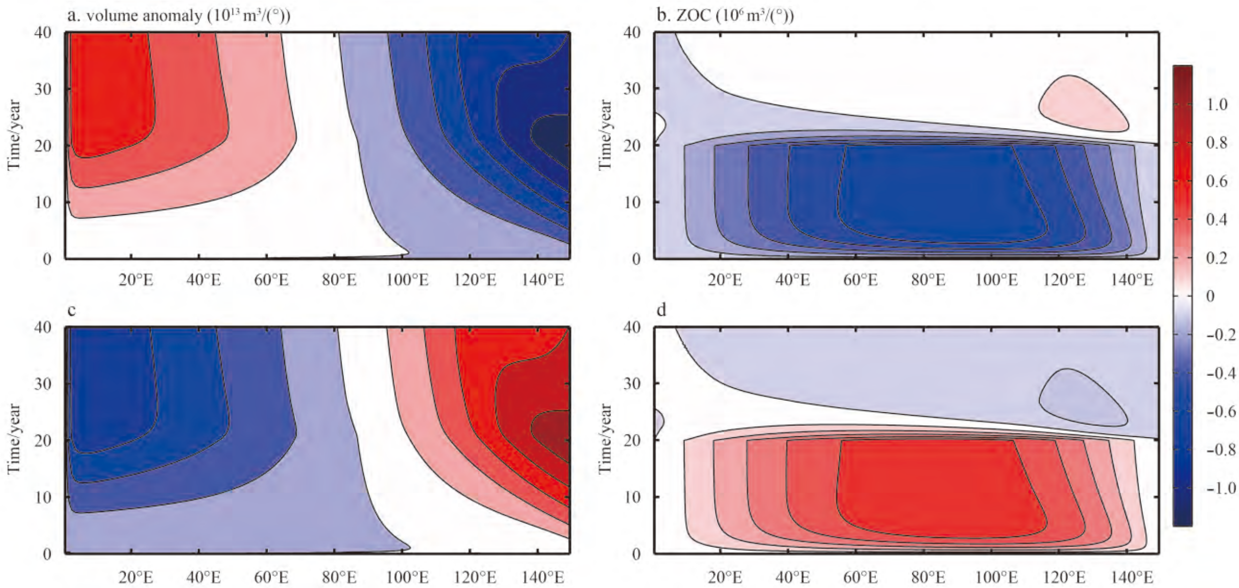

Fig. 5. Time evolution of the oceanic response in Exp. 2H-A (top panels) and Exp. 2H-B (lower panels). The left panels for volume anomaly, and right panels for the strength of ZOC.

Table 2. Wind stress perturbations applied in the numerical experiments

		Exp. number							
		2H-A	2H-B	2H-C	2H-D	2H-E	2H-F	2H-G	2H-H
Two-hemisphere model	latitude of zonal wind perturbations (Fig. 4)	equator	equator	20°N	40°N	60°N	20°S/20°N	40°S/40°N	60°S/60°N
		Exp. number							
		SH-E	SH-G						
Southern Hemisphere model	center of zonal wind perturbations (Fig. 12)	(0°S, 180°E)	(30°S, 180°E)						

ward, the negative volume anomaly near the eastern boundary declines slightly and gradually. Compared with the eastern basin, the volume increase in the western basin reaches the peak with several years lag, and the amplitude of the maximum remains nearly constant. The zonal profile of the volume anomaly at the end of the 40 year simulation is shown in Fig. 6a (blue curve). A steep gradient of volume anomaly near the western boundary implies an enhancement of the western boundary current.

In a steady state of wind-driven circulation there is no net meridional or zonal volume transport. In a transit state, there is a new phenomenon, the horizontal heat flux induced by adiabatic motions, as discussed by Huang (2015). By definition, the lower layer in a reduced gravity model is assumed motionless. However, sea level in the ocean must remain nearly constant, within the order of one meter; thus, the large volume of westward transportation in the upper layer should be compensated by the eastward return flow in the lower layer. As such, the zonal transport of warm water in the upper layer of a reduced gravity model leads to an equivalent anomalous ZOC, which is defined as follows

$$M_{\mathrm{ZOC}}(x,t)=\int_{y_s}^{y_n} u(x,y,t)\,h(x,y,t)\,\mathrm{d}y\,, \tag{5}$$

where y_s and y_n are the southern and northern boundaries, and u is the zonal velocity.

In this paper, the ZOC associated with an eastward flow in the upper layer is defined as positive. In Fig. 5b, the negative ZOC appearing immediately in response to the onset of the anomalous easterly indicates a westward flow in the upper layer. As discussed above, to maintain the sea level at each station nearly constant, there should be a return flow beneath the upper layer, i.e., the westward flow in the upper layer implies an eastward return flow in the lower layer. The maximum magnitude (-0.59×10^6 m^3/s) occurs in the central basin; after the wind stress perturbations reach the peak value and increase no more, the negative ZOC diminishes rapidly and it changes into a positive ZOC with a rather small amplitude. A close examination of the ZOC shown in Fig. 5b reveals that the amplitude of the ZOC reaches its maximum around year 5, well before the wind stress perturbations reach the full-scale amplitude. Apparently, the ZOC amplitude overshoots and oscillates; the oscillation of ZOC is quite similar to the oscillation of MOC, and it is obviously linked to the movement of Rossby and Kelvin waves in the model basin, as discussed by many investigators, e.g., Huang (2015) and the references therein.

The 40 years averaged ZOC is negative in the whole basin, and the extreme is close to -0.3×10^6 m^3/s in the central basin (Fig. 6b, blue curve). Note that the maximum amplitude of ZOC (0.3×10^6 m^3/s) is comparable with that of MOC (0.2×10^6 m^3/s) associated with the same experiment (Fig. 6d in Huang 2015), implying that the zonal adiabatic adjustment is important as well and should not be neglected.

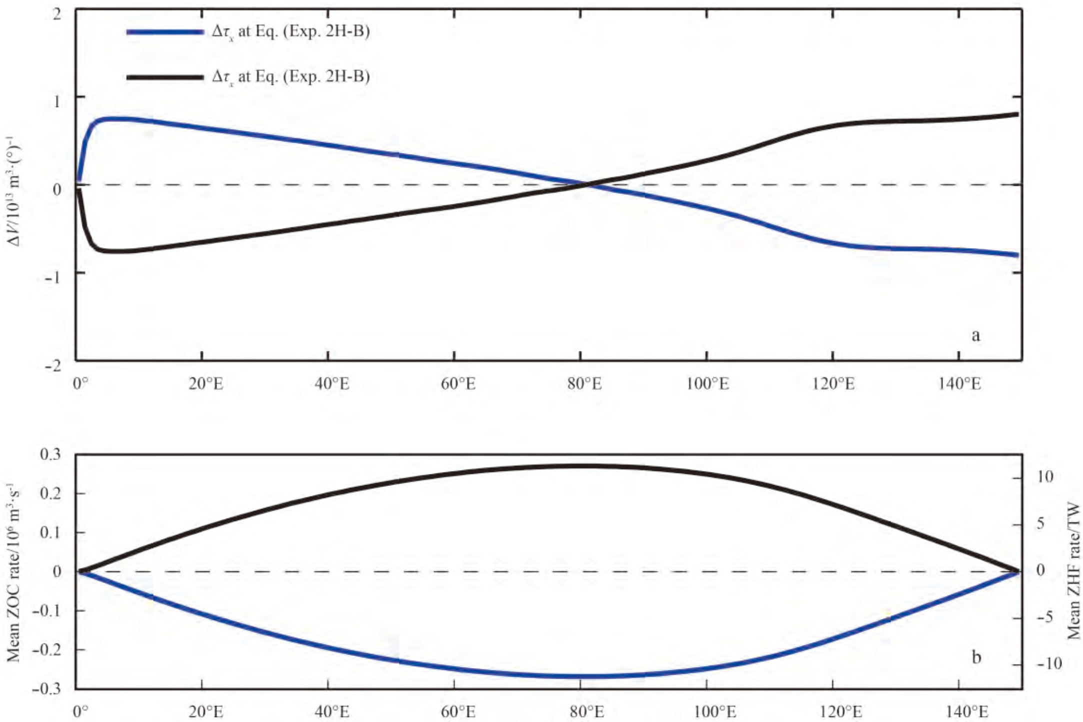

Fig. 6. Zonal distribution of the volume anomaly (ΔV) at the end of the simulation (a) and ZOC (ZHF) averaged over 40 years (b) in Exp. 2H-A (blue curve) and Exp. 2H-B (black curve).

Since the ZOC is associated with zonal transport of warm water in the upper layer and the compensating return flow of the cold water in the lower layer, there is a critically important quantity in connection with ZOC: the ZHF, which is defined as

$$H_{\mathrm{ZOC}}(x,t)=\int_{y_{\mathrm{s}}}^{y_{\mathrm{n}}}\rho_0 C_p \Delta T u(x,y,t)\,h(x,y,t)\mathrm{d}y\,, \qquad (6)$$

in which ρ_0=1 035 kg/m^3 is the sea water density in the upper layer, C_p = 4 186 J/(kg·°C) is the specific heat capacity at constant pressure, and ΔT = 10°C is the temperature difference between two layers in this model ocean. Since all these three parameters are constant, the ZHF profile is the same as that of ZOC, except for a different unit, as shown by the y-coordinate on the right hand side of Fig. 6b. In this experiment (2H-A), the 40 year mean westward heat flux has a maximum value of –11.2 TW (1 TW = 10^{12} W).

In Exp. 2H-B, the positive zonal wind stress perturbations applied to the equatorial band, i.e., the equatorial easterly is reduced (Fig. 4a). Since the amplitude of the perturbations is relatively small, the ocean response is almost linear with respect to the wind stress (including its sign), the corresponding volume anomaly (Fig. 5c, black curve in Fig. 6a) and ZOC (Fig. 5d, black curve in Fig. 6b) in Exp. 2H-B are the same as those in Exp. 2H-A, except with the opposite sign.

2.4 *Simulations with wind stress perturbations at one latitudinal band*

In order to investigate the ocean responses to wind stress perturbations at other latitudes, we present results from 3 other experiments (Exp. 2H-C, Exp. 2H-D and Exp. 2H-E) forced by positive wind stress perturbations applied to 20°N, 40°N and 60°N (Fig. 4b).

In Exp. 2H-C, positive zonal wind stress perturbations applied to 20°N weaken the Ekman pumping around latitude band of 20°–30°N. In opposite to the sketch shown in Fig. 2, weakening of Ekman pumping induces a reduction of the thermocline slope in the subtropical gyre and thus leads to warming of the eastern basin. As a result, this gives rise to the volume anomaly (Fig. 7c) showing a pattern similar to that in Exp. 2H-B (Fig. 7a). There are some minor differences in terms of the time when the volume anomaly extrema appear. In Exp. 2H-B, the volume anomaly maximum near the eastern boundary occurs at year 20, while it appears in year 30 in Exp. 2H-C. On the other hand, negative volume anomaly near the western boundary reaches its peak near year 25 in Exp. 2H-B, and gradually shrinks afterward; however, the corresponding negative anomaly in Exp. 2H-C appears at the end of the 40 year experiment. Such a time-lag may be mainly due to the fact that thermocline near 20°N is deeper than along the equator (Fig. 3b), especially in the western basin.

Due to such differences, in Exp. 2H-C the ZOC remains mostly positive after the wind stress perturbations reach the full scale and increase no more (Fig. 7d), whereas in Exp. 2H-B, the ZOC reverses right after wind stress perturbation reaches its peak value (Fig. 7b).

Exp. 2H-D is quite interesting. In this experiment, the wind stress is increased in the 40°N, which implies a stronger Ekman pumping for the subtropical gyre and a stronger Ekman suction in the subpolar gyre. Thus, warm water is pushed down in the subtropical basin interior, but it is pushed upward in the subpolar basin interior. The thermocline depth at the end of 40 year experiment is shown in Fig. 8a. Thermocline along 40°N is nearly constant because this is the latitude of maximum wind stress, so that the Ekman pumping rate is nearly zero. The bowl-shaped thermocline south of this latitude is clearly shown in this figure. Within the subpolar gyre, the thermocline is in a dome shape; in

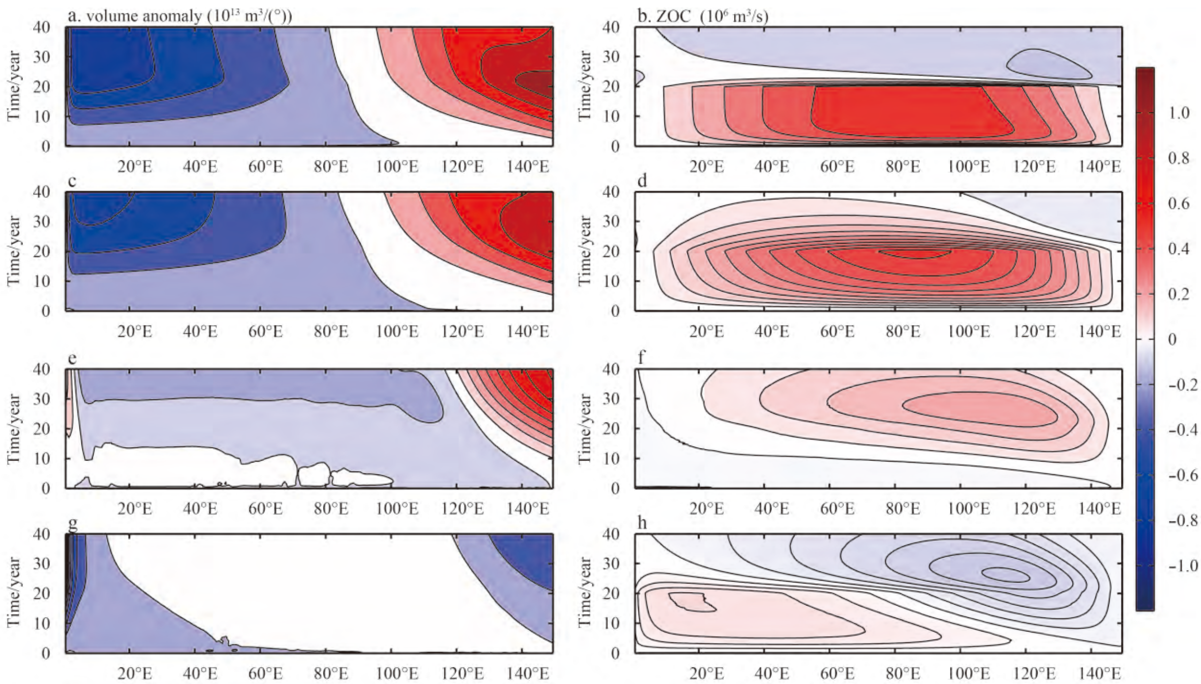

Fig. 7. Time evolution of the oceanic response in Exp. 2H-B (the top row), Exp. 2H-C (the second row), Exp. 2H-D (the third row) and Exp. 2H-E (the bottom row). The left panels for volume anomaly (a, c, e, g), and right panels for ZOC (b, d, f, h).

fact, the thermocline depth is nearly zero within the center of the subpolar gyre. The strong Gulf Stream like western boundary current after separation is manifested as a shape layer depth front between 40° and 50°N as shown in Fig. 8a.

Within the framework of this simple reduced gravity model on a beta-plane, loss of warm water in the subpolar basin interior overpowers the gain of warm water in the subtropical basin interior. As a result, thermocline depth along the eastern boundary is increased approximately 4.8 m, and shown in Fig. 8b. Although layer depth within the subtropical basin interior increases (such as along 10°, 20°, and 30°N; magenta, dashed blue and green curves in Fig. 8b), layer depth along 40°, 50° and 60°N is reduced greatly, red, blue and black curves in Fig. 8b.

Note that the volume anomaly at the end of the simulation along with 40-year averaged ZOC in both Exp. 2H-B and Exp. 2H-C share virtually the same profile (black and blue curves in Fig. 9). This fact is, however, merely coincident; when the model runs for a longer time, the mean ZOC can be different.

Compared with Exp. 2H-B and Exp. 2H-C, the positive volume anomaly in Exp. 2H-D is mostly confined to the eastern boundary, and the negative anomaly occupies in the western and central basins with much smaller amplitude (Fig. 7e and the red curve in Fig. 9a). It is noted that the maximum magnitude of either positive or negative volume anomaly appears at the end of the simulation. The corresponding ZOC is always positive during the whole time period (Fig. 7f), even at the end of simulation. It seems that if the experiment continues to run for longer time, the amplitude of positive and negative volume anomaly may increases further. Due to zonal shift of the positive volume anomaly, the maximum magnitude of the mean ZOC associated with the ZHF locates father eastward and the corresponding amplitude is much smaller for the most part of the basin (0.13×10^6 m^3/s for ZOC, and 5.35 TW for ZHF) than that in Exp. 2H-B and Exp. 2H-C (Fig. 9b).

In Exp. 2H-E, the positive wind stress perturbations applied to 60°N give rise to weakening of the Ekman sucking in the latitude

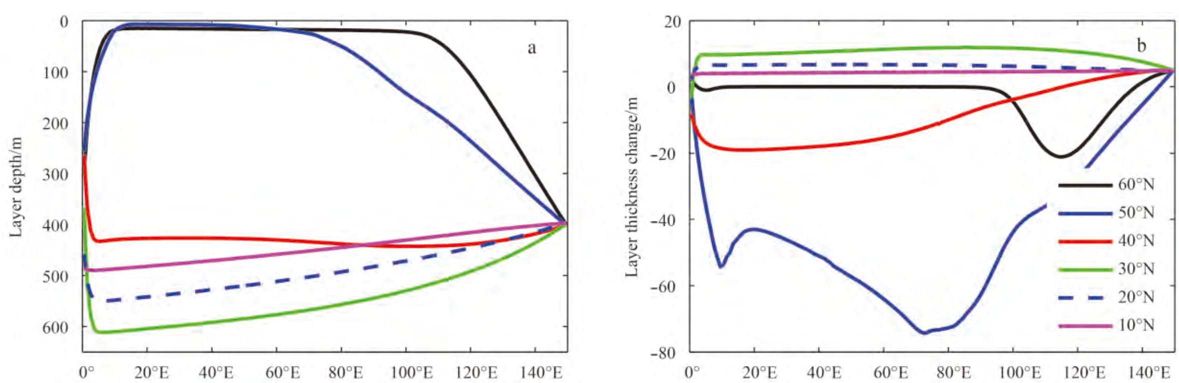

Fig. 8. The zonal profiles of thermocline depth (a) and its perturbations (b) in Exp. 2H-D.

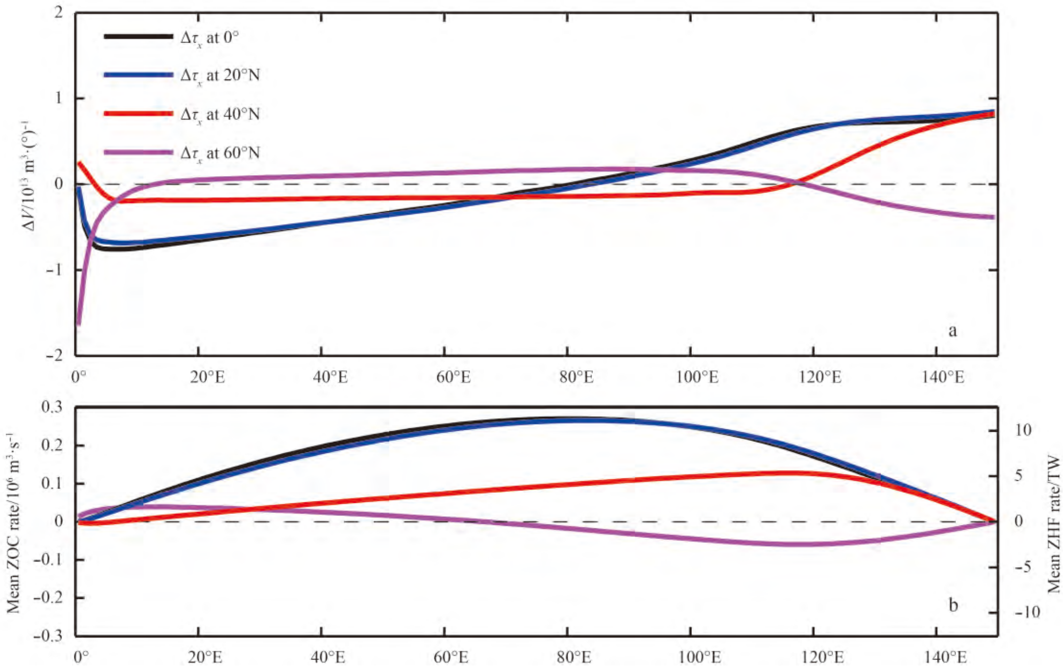

Fig. 9. Zonal distribution of the volume anomaly at the end of the simulation (a) and ZOC (ZHF) averaged over 40 years (b) in Exp. 2H-B (black curve), Exp. 2H-C (blue curve), Exp. 2H-D (red curve) and Exp. 2H-E (magenta curve).

band of 50°–60°N. Similar to the sketch shown in Fig. 2, weakening of the Ekman sucking in the subpolar basin induces a flattening of the dome-shaped thermocline in the subpolar gyre. As a result, thermocline near the eastern boundary shoals, which is reflected as cooling near the eastern boundary, Fig. 7g. However, in this case the oceanic response has much smaller amplitude. Although the volume decreases near the eastern and western boundary, it increases in the middle basin, which amplitude is so small that it is almost invisible in the color map for most of the basin (Fig. 7g); nevertheless, the corresponding profile at the end of the experiment is clearly shown by the magenta curve in Fig. 9a. Accordingly, the ZOC is weak: during the first 20 years when the wind stress perturbations increase, it is small and positive, except for a small region near the eastern boundary; after the wind stress perturbations reach the full scale and increase no more, the ZOC becomes negative, except for a very small part of the model ocean next to the western boundary (Fig. 7h). The volume anomaly profile at the end of the experiment is shown as the magenta curve in Fig. 9a, and the corresponding ZOC and ZHF profiles averaged over the 40 year experiment is shown as the magenta curve in Fig. 9b.

2.5 *Simulations with symmetric wind stress perturbations*

In this section, positive wind stress perturbations symmetric to the equator are imposed on 20°N/20°S, 40°N/40°S and 60°N/60°S respectively (Fig. 4c); these experiments are labeled as Exp. 2H-F, Exp. 2H-G and Exp. 2H-H. As discussed above, the oceanic response is linear with respect to the wind stress perturbation, if the wind stress perturbations have small amplitude; thus, the zonal adjustments of the symmetric simulations are almost double of those in Exp. 2H-C, Exp. 2H-D and Exp. 2H-E (Fig. 10). It is no doubt that the volume anomaly and ZOC would be close to 0 in response to asymmetric wind stress perturbations (figure not shown).

3 A Southern Hemisphere model ocean

In the Southern Hemisphere, wind-driven circulation shows some extraordinary characteristics due to the existence of the Antarctic Circumpolar Current (ACC) connecting the three subbasins (the Indian basin, Pacific basin and Atlantic basin). Besides the inter-gyre heaving modes for a single basin described in Section 2, there are two new modes: the annular mode and interbasin mode, as discussed in Huang (2015). In the following discussion our focus is on the anomalous ZOC and ZHF associated with the inter-basin heaving mode.

3.1 *Model set up*

Similar to the 2H model, the Southern Hemisphere (SH) model is also a reduced gravity model, but with 3 sub-basins connected through the ACC in the southern hemisphere. The model is 360° wide in the longitude, and extends from 60°S to the equator. A 15° wide periodic channel representing ACC exists near the southern edge from 60° to 45°S. North of 45°S, the model ocean is separated into 3 sub-basins by 3 continents: the Indian basin is 60° wide (15°E to 75°E), the Pacific basin is 150° wide (105°E to 105°W), and the Atlantic basin is 60° wide (75° to 15°W), respectively. In the model, the connections between the Pacific and Indian Ocean via the Indonesian Throughflow are excluded.

The SH model is also based on an equatorial β-plane, and all the parameters are set according to Huang (2015), $\beta = 2.1\times10^{-11}$ m^{-1}·s^{-1}, g'=0.01 m/s^2, and the temperature difference between two layers is set to 7.5°C, Table 1. In addition, the zonal wind stress applied in the SH model is diagnosed from 51 year averaged zonal wind stress of SODA 2.1.6 data (Carton and Giese, 2008). Because thermocline in the Southern Oceans is quite deep, we set the initial depth of the main thermocline at 750 m. The model is started from an initial state of rest with the thermocline at a constant depth of 750 m, and the model was run for 300 years to reach a quasi-equilibrium state. The zonal wind stress profile, the thermocline depth and streamfunction at this quasi-

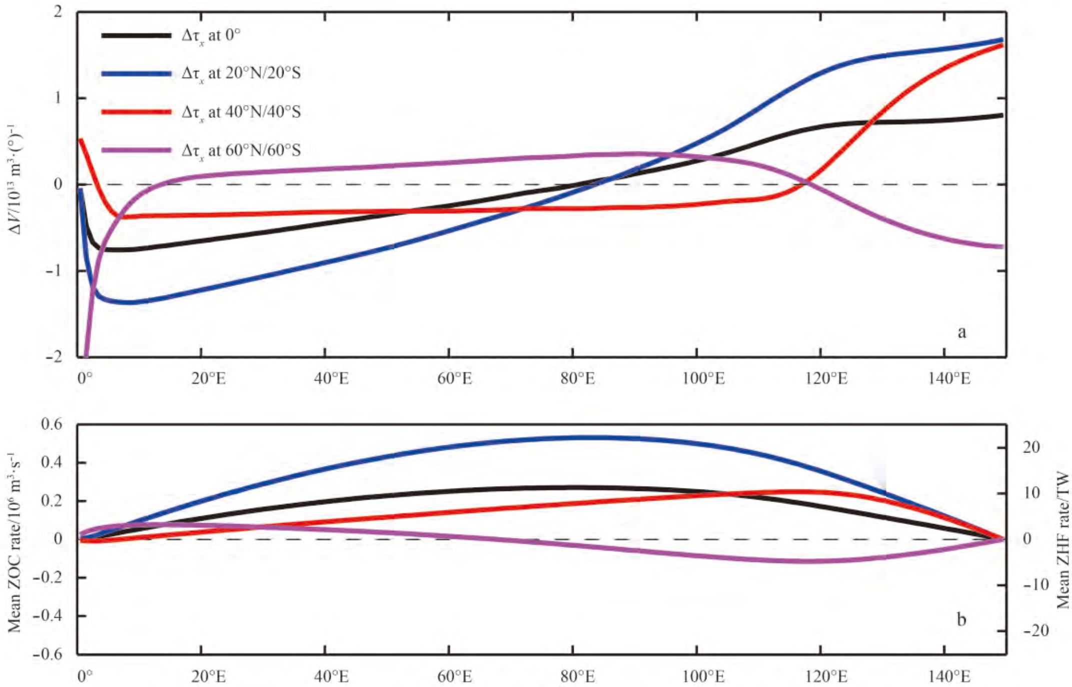

Fig. 10. Zonal distribution of the volume anomaly at the end of the simulation (a) and ZOC (ZHF) averaged over 40 years (b) in Exp. 2H-B (black curve), Exp. 2H-F (blue curve), Exp. 2H-G (red curve) and Exp. 2H-H (magenta curve).

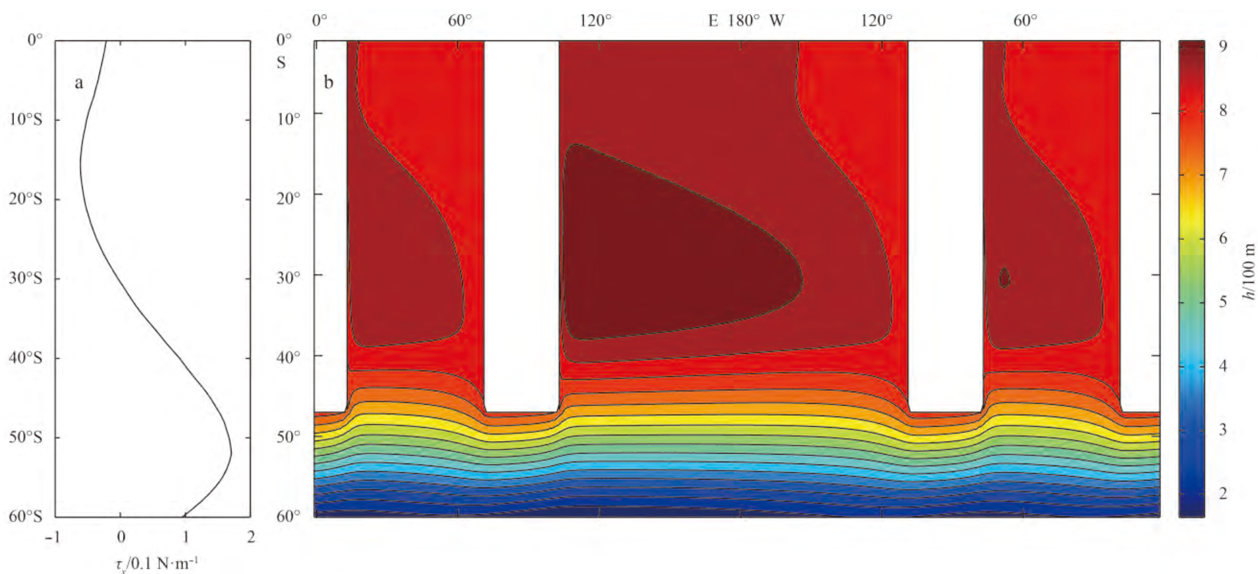

Fig. 11. The quasi-equilibrium state used in the SH model: a. the zonal wind stress; and b. the depth of the main thermocline.

equilibrium state are shown in Fig. 11. Note that due to the simplification nature of a reduced gravity model, the thermocline depth in the model is not very accurate, compared with observations. Nevertheless, we hope this simple model can be used to illustrate the basic ideas related to ZOC, ZHF and other dynamic concepts associated with the circulation in the Southern Oceans.

3.2 *Simulations with wind stress perturbations in the Pacific basin*

In order to explore the inter-basin heaving mode in response to the wind stress perturbations applied to individual basins, two numerical experiments are restarted from the above mentioned quasi-equilibrium state and driven by additional small wind stress perturbations

$$\tau'_x = \Delta\tau e^{-[(x-x_0)/\Delta x]^2-[(y-y_0)/\Delta y]^2}, \quad (9)$$

where $\Delta\tau$=0.02 N/m^2, Δx=3 300 km, Δy=1 100 km, (x_0, y_0) are the longitude and latitude of the center of perturbations. In Exp. SH-E, the center is located at (0°S, 180°E) in the Pacific basin, and in Exp. SH-G, it is at (30°S, 180°E), Fig. 12 and Table 2. In these two experiments, wind stress perturbations are both linearly in-

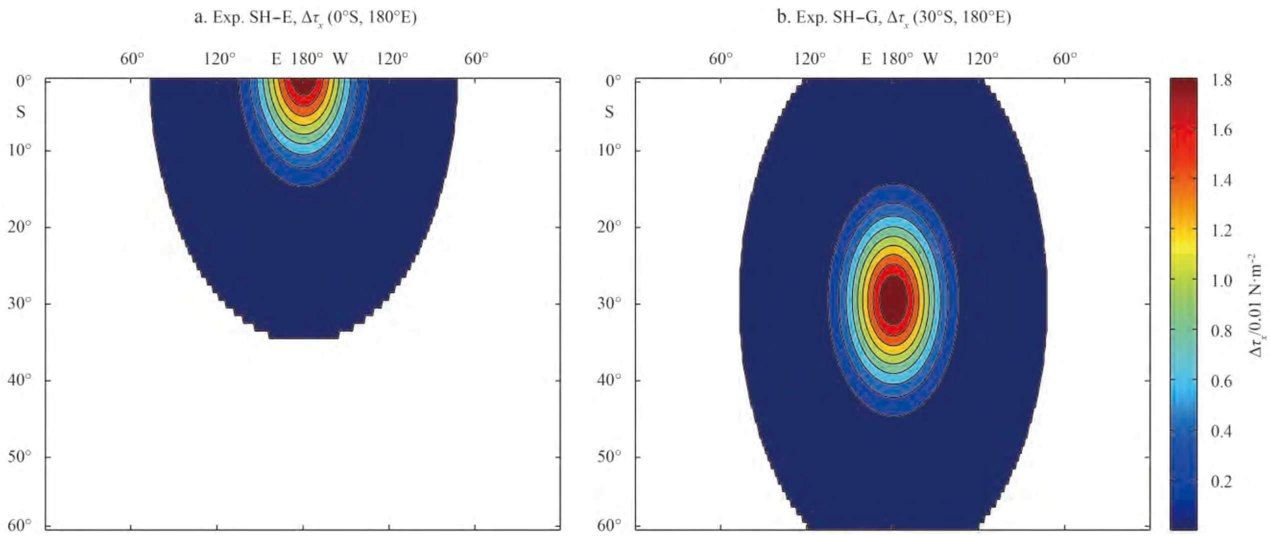

Fig. 12. Zonal wind stress perturbations used in Exps SH-E and SH-G.

creased from 0 at the beginning to the specified magnitude (Eq. (9)) at the end of 20 years. Afterward, there are no further changes in wind stress and the model runs for additional 100 years. Note that the labelling of these experiments is the same as discussed in Huang (2015); thus, the readers can find out the relevant information of these two experiments, such as the MOC, PHF, the vertical heat flux, in Huang (2015).

In the following discussion our focus is on the time evolution of the ZOC and ZHF for each individual sub-basin north of the ACC. In Exp. SH-E, positive wind stress anomalies are imposed on the equator in the Pacific basin. Due to the weakening of the equatorial easterly, part of the warm water piled up in the warm pool in the western Equatorial Pacific moves eastward; thus, the fastest response occurs in the Pacific with positive (negative) volume anomaly east (west) of 180°E, and it lasts until the end of the simulation (Fig. 13a). The positive volume anomaly reaches its maximum at the eastern boundary in year 20, and it declines afterward.

Accordingly, the ZOC in most part of the Pacific basin flows eastward from the beginning to year 20, except for a narrow region near the western boundary where a narrow negative overturning cell exists, as shown in the middle of Fig. 13b. After year 20, the positive volume anomaly near the eastern boundary starts to decline; thus, the corresponding ZOC becomes negative for the whole Pacific basin.

It should be noted that the loss of warm water in the western Pacific is greater than the increase in the eastern Pacific, leading to a net volume of warm water decrease in the Pacific basin (Fig. 13a). Such a reduction of warm water in the Pacific basin should be compensated in other two basins through ACC. The adjustment in the Atlantic is secondary, the significant positive volume anomaly appears from year 20 to the end of the experiment in the Atlantic, and the positive ZOC appears from year 6 to year 40. The response in the Indian Ocean appears the latest (Fig. 13a), mainly because the Indian Ocean is located downstream of the ACC, and the corresponding ZOC is positive during almost the whole simulation (except in the first 5 years) with an invisibly small amplitude (Fig. 13b). It should be noted that negative volume anom-

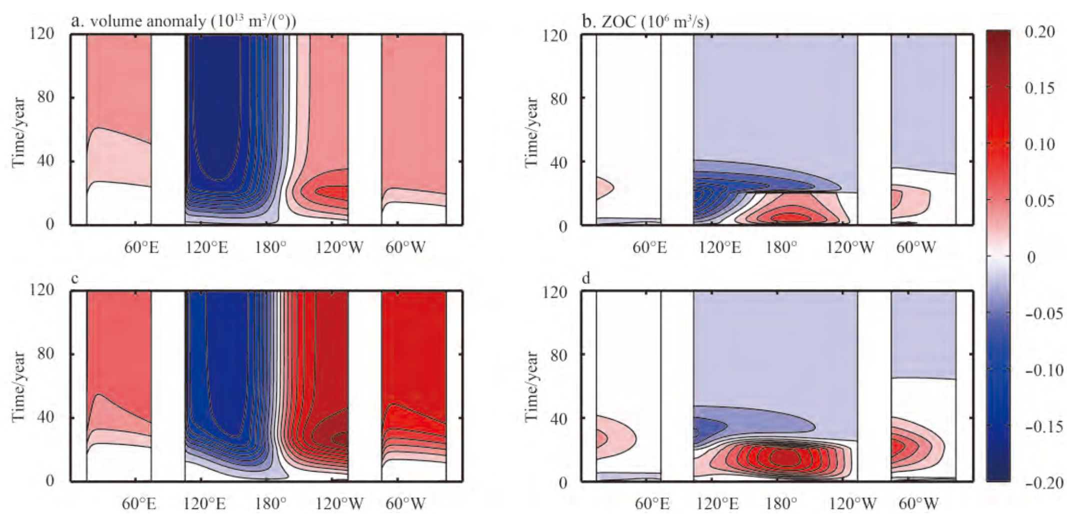

Fig. 13. Time evolution of the oceanic response in Exp. SH-E (the top row) and Exp. SH-G (the bottom row); the left panels for volume anomaly (a, c), and right panels for ZOC (b, d).

aly appears near the eastern boundary of the Atlantic and Indian Oceans in the first 5 years, with invisible amplitude; the decline in warm water in the eastern part of these sub-basins corresponds to negative (westward) ZOC; these cells can be barely seen above the horizontal axis in Fig. 13b.

In Exp. SH-G, the positive zonal wind stress perturbation center is located at 30°S, and such wind stress perturbations give rise to a weakened Ekman pumping in the subtropical South Pacific basin. As shown in the sketch in Fig. 2, the weakening of Ekman pumping induces a decline of the thermocline slope. As a result, warm water above the thermocline moves eastward, leading to warming in the eastern basin and cooling in the western basin. In comparison with Exp. SH-E, more ocean areas are influenced by the anomalous wind stress in the present case; thus, the amplitudes of volume anomaly in three sub-basins are much larger than those in Exp. SH-E (Fig. 13c). Nevertheless, the time evolution of the anomalous ZOC is quite similar to the case in Exp. SH-E, as shown in Fig. 13d.

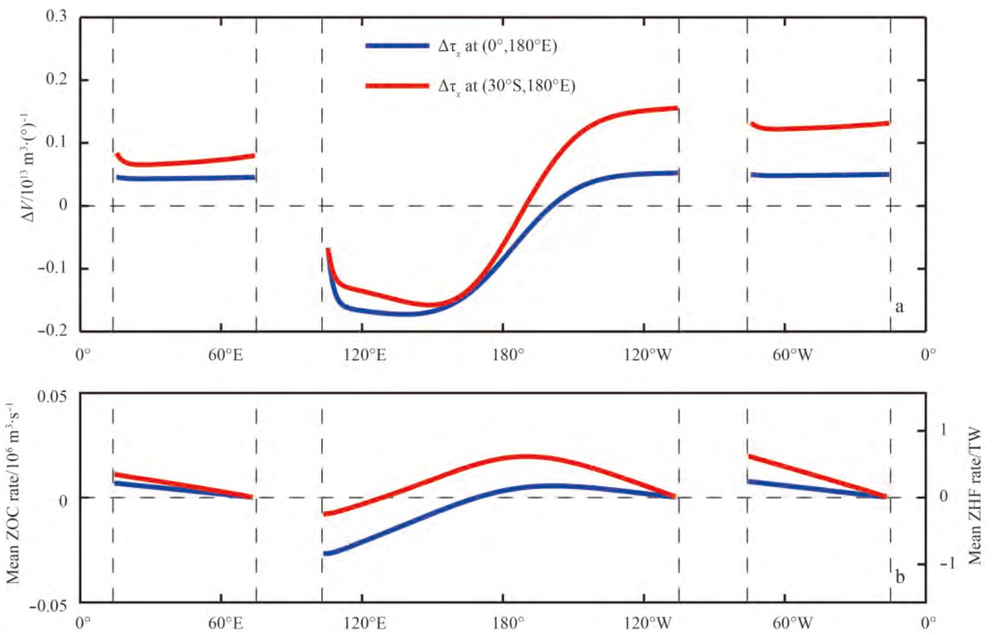

Fig. 14. Zonal distribution of the volume anomaly at the end of the simulation (a) and ZOC (ZHF) averaged over 120 years (b) in Exp. SH-E (blue curve) and Exp. SH-G (red curve).

The zonal profiles of volume anomaly at the end of the 120 year run are exhibited in Fig. 14a, which is consistent with the time evolutions in Fig. 13. In general the eastern Pacific gains warm water, but the western Pacific loses warm water. Since the warm water volume decrease in the western Pacific overpowers the gain in the eastern pacific, both the Atlantic and Indian basins gain warm water, as shown in Fig. 14a.

The corresponding ZOC and ZHF are shown in Fig. 14b. In the eastern Pacific basin, the ZOC (ZHF) is positive. This reflects the fact that there is an eastward transport of warm water in the upper layer. In fact, for Exp. SH-G both ZOC and ZHF are positive for most part of the Pacific basin; while, in Exp. SH-E both ZOC and ZHF are negative west of the dateline. The ZOC in both the Atlantic and Indian basins have small positive values, Fig. 14b.

4 Conclusions

Meridional overturning circulation and the associated poleward heat flux have been studied extensively because of their vital role in climate system and global climate change. In most of previous studies, MOC and PHF were examined mostly from the angle of thermohaline circulation and its variability. However, Huang (2015) postulated a different view of these two climate components and suggested that on decadal time scales heaving motions induced by decadal wind stress changes can also make sizeable contributions to the variability of MOC and PHF.

As an obvious extension of this basic idea, we demonstrated that heaving motions in the world oceans can also induce sizable variability of ZOC and ZHF; thus, they should be examined carefully in the study of oceanic general circulation and climate variability. It is obvious that the simple model used in our study may not be able to provide accurate description of heaving motions in the world oceans; nevertheless, we hope the basic ideas illustrated by our simple model may stimulate further study along this line of thought.

Acknowledgements

Tan Wei sincerely thanks for the continuous support from Zuo Juncheng during his study. Suggestions from two anonymous reviewers helped to improve the presentation greatly.

References

Behringer D W, Ji M, Leetmaa A. 1998. An improved coupled model for ENSO prediction and implications for ocean initialization. Part I: The ocean data assimilation system. Mon Wea Rev, 126(4): 1013–1021

Bindoff N L, McDougall T J. 1994. Diagnosing climate change and ocean ventilation using hydrographic data. J Phys Oceanogr, 24(6): 1137–1152

Carton J A, Giese B S. 2008. A reanalysis of ocean climate using Simple Ocean Data Assimilation (SODA). Mon Wea Rev, 136(8): 2999–3017

England M H, McGregor S, Spence P, et al. 2014. Recent intensifica-

tion of wind-driven circulation in the Pacific and the ongoing warming hiatus. Nature Climate Change, 4(3): 222–227
Ganachaud A, Wunsch C. 2000. Improved estimates of global ocean circulation, heat transport and mixing from hydrographic data. Nature, 408(6811): 453–457
Huang R X. 1987. A three-layer model for wind-driven circulation in a subtropical-subpolar basin. Part I: Model formulation and the Subcritical state. J Phys Oceanogr, 17(5): 664–678
Huang R X. 2010. Ocean Circulation: Wind-driven and Thermohaline Processes. Cambridge: Cambridge University Press, 791
Huang R X. 2015. Heaving modes in the world oceans. Climate Dynamics, doi: 10.1007/s00382-015-2557-6
Lozier M S, Leadbetter S, Williams R G, et al. 2008. The spatial pattern and mechanisms of heat-content change in the North Atlantic. Science, 319(5864): 800–803
Lozier M S, Roussenov V, Reed M S C, et al. 2010. Opposing decadal changes for the North Atlantic meridional overturning circulation. Nat Geosci, 3: 728–734
Lyman J M, Johnson G C. 2008. Estimating annual global upper-ocean heat content anomalies despite irregular in situ sampling. J Climate, 21(21): 5629–5641
McGregor S, Sen Gupta A, England M H. 2012. Constraining wind stress products with sea surface height observations and implications for Pacific Ocean sea level trend attribution. J Climate, 25(23): 8164–8176
Meehl G A, Arblaster J M, Fasullo J T, et al. 2011. Model-based evidence of deep-ocean heat uptake during surface-temperature hiatus periods. Nature Climate Change, 1: 360–364
Meehl G A, Hu A X, Arblaster J M, et al. 2013. Externally forced and internally generated decadal climate variability associated with the Interdecadal Pacific Oscillation. J Climate, 26(18): 7298–7310
Schmitz W J Jr. 1986a. On the world ocean circulation: Volume I, Some global features/North Atlantic circulation. Woods Hole Oceanographic Institution Technical Report WHOI-96-03, 148
Schmitz W J Jr. 1986b. On the world ocean circulation: Volume II, the Pacific and Indian Oceans/A global update. Woods Hole Oceanographic Institution Technical Report WHOI-96-08, 241
Talley L D. 2013. Closure of the global overturning circulation through the Indian, Pacific, and Southern Oceans: Schematics and transports. Oceanography, 26: 80–97
Talley L D, Pickard G L, Emery W J, et al. 2011. Descriptive Physical Oceanography: An Introduction (Sixth Edition). Boston: Elsevier, 560